

Spatial mapping of disordered 2D materials: the conductance Sudoku

S. Mukim,^{1,2} C. Lewenkopf,³ and M. S. Ferreira^{1,2}

¹*School of Physics, Trinity College Dublin, Dublin 2, Ireland*

²*Centre for Research on Adaptive Nanostructures and Nanodevices (CRANN) & Advanced Materials and Bioengineering Research (AMBER) Centre, Trinity College Dublin, Dublin 2, Ireland*

³*Instituto de Física, Universidade Federal Fluminense, 24210-346 Niterói, Brazil*

(Dated: February 28, 2022)

Motivated by recent advances on local conductance measurement techniques at the nanoscale, timely questions are being raised about what possible information can be extracted from a disordered material by selectively interrogating its transport properties. Here we demonstrate how an inversion technique originally developed to identify the number of scatterers in a quantum device can be adapted to a multi-terminal setup in order to provide detailed information about the spatial distribution of impurities on the surface of a 2D material. The methodology input are conductance readings (for instance, as a function of the chemical potential) between different electrode pairs, the output being the spatially resolved impurity density. We show that the obtained spatial resolution depends not only on the number of conductance measurements but also on the electrode dimensions. Furthermore, when implemented with electrodes in a grid-like geometry, this inversion procedure resembles a Sudoku puzzle in which the compositions of different sectors of a device are found by imposing that they must add up to specific constrained values established for the grid rows and columns. We argue that this technique may be used with other quantities besides the conductance, paving the way to alternative new ways of extracting information from a disordered material through the selective probing of local quantities.

Inverse Problems (IP) in science are those that attempt to obtain from a set of observations the causal factors that generated them in the first place. IP are intrinsic parts of several visualization tools [1–4] but are far less ubiquitous in the quantum realm. In fact, the literature on the field of Quantum IP (QIP) is centred heavily on the fundamentals of inversion processes, e.g. whether a problem is ill-posed [5], whether solutions are unique, stable [6], etc. In contrast, Materials Science appears as fertile ground for applications of QIP since it involves studying the physical properties of structures for which the underlying Hamiltonians are often unknown [7–14].

Finding the precise parent Hamiltonian that generates a specific observable is an arduous process. In general, it consists of solving the Schrödinger equation with a Hamiltonian containing one (or more) variable parameter(s) which are varied until the solution closely matches the original observation. Because of the enormous number of possibilities, finding the exact configuration may be a computationally demanding task. It is worth stating that efficient codes and powerful computers alone are not sufficient to make this approach feasible and alternative ways of probing the phase space of possibilities are required. Neural-network-based search engines [15, 16], genetic algorithms [17] and, more recently, machine-learning strategies [18–27] have been proposed and, with different degrees of success, can speed up the search for the "inverted" configuration. As a result, simulations are starting to have an impact in reducing the time and cost associated with materials design, specially those involving high throughput studies of material groups [28–36]. These are large scale simulations that generate a gigantic volume of data with the intention of identifying optimal

combinations that can be subsequently used as candidates for an exploratory experimental search of new materials. Despite the advances offered by these approaches, so far they are all based on "black-box" algorithms that bring little insight into the problems they aim to address [37]. Moreover, it should be stressed that disorder effects, that are ubiquitous in real systems, have not been addressed by this line of research.

In a recent communication [38], an inversion technique capable of extracting structural and compositional information from a disordered quantum device by analysing its electronic transport properties has been proposed. Using the energy-dependent two-terminal conductance as the sole input, the reported inversion method identifies the exact number of impurities within the disordered material. Furthermore, it is particularly suitable to be used in 2D materials, is very stable and works in the ballistic, diffusive as well as at the onset of the localised transport regimes. While the ability to determine the precise number of impurities in a device through conductance inversion is in itself a significant achievement, the referred technique is not able to capture the spatial distribution of impurities but only the average concentration between a pair of electrodes. In this manuscript, we demonstrate how the two-terminal inversion technique can be adapted to handle a multi-terminal disordered device. Interestingly, this generalisation gives enormous flexibility to how a disordered structure can be interrogated and, in doing so, leads to an inversion tool that obtains spatial information about the impurity concentration, something that Ref. [38] lacked. Remarkably, when implemented in a grid-like geometry, the inversion procedure resembles a Sudoku puzzle in which the compositions of different

sectors of a device are obtained by imposing that they must add up to specific values established for the grid rows and columns.

The experimental setup required to implement our proposal can be easily realised with current nanoscale fabrication techniques. Multi-terminal experiments have played a key role in the understanding of the electronic transport properties of a variety of 2D systems [39, 40] (see, *e.g.*, Ref. [41] for a detailed discussion). Through multiple measurements of local and non-local resistances [42], one can in principle experimentally determine the multiterminal conductance matrix. The possibilities have been vastly improved by techniques that enable to directly probe the local conductances at the nanoscale such as scanning gate microscopy [43–46] and multi-probe scanning tunneling spectroscopy [47, 48], to name but a few. These recent experimental developments provide extra motivation to explore what type of information can be obtained from a disordered device through selectively interrogating its transport properties, which is precisely the underlying idea behind this work.

This manuscript is structured as follows: We begin presenting the inversion methodology in a multi-electrode framework and applying it first to an illustrative case in which the impurity concentration is captured as a whole but not spatially resolved. Subsequently, we demonstrate how the same inversion tool can be implemented to extract information about the spatial distribution of impurities from the conductance between terminals, sampling the electronic transport flow at different parts of the device. This will be done for a few different cases where the device is divided into a number of cells that determines the spatial resolution of the inversion.

Fig. 1(a) shows a schematic diagram of the multi-terminal setup considered here. It consists of a 2D material system connected to multiple electrodes represented by the coloured stripes labelled L_1 to L_4 . Although the electrodes shown in Fig. 1(a) span the full length of the device, only partial sections of their length may be used to inject and extract current as discussed below. The sheet contains a finite number of randomly distributed impurities represented by red dots, here assumed to represent substitutional atoms other than those of the host 2D material. Adsorbed impurities [49] or vacancies [50] can be easily considered as well. In this paper, due to its relevance and model simplicity [51], we choose a graphene sheet as a case in point. We stress that the inversion methodology is also applicable to other 2D materials, see for instance Ref. 52.

In linear response theory, the multi-terminal Landauer-Büttiker formula for the electronic current I_j at the terminal j reads [41, 42, 53, 54]

$$I_j = \sum_{\ell=1}^N \mathcal{G}_{j\ell} (V_j - V_\ell), \quad (1)$$

where V_j is the voltage applied to the j -terminal and $\mathcal{G}_{j\ell}$ is the conductance given by

$$\mathcal{G}_{j\ell} = \frac{2e^2}{h} \int_{-\infty}^{\infty} dE \left(-\frac{\partial f}{\partial E} \right) \mathcal{T}_{j\ell}(E) \quad (2)$$

expressed in terms of the the Fermi distribution $f(E) = [1 + e^{(E-\mu)/k_B T}]^{-1}$ and the transmission coefficient $\mathcal{T}_{j\ell}(E)$. The factor 2 assumes spin degeneracy. The conductance $\mathcal{G}_{j\ell}$ is a function of the chemical potential μ and, in principle, can be either calculated or measured experimentally with the assistance of external gate voltages. For the purposes of this manuscript, we shall concentrate on the former for the simple fact that it is then a straightforward task to test the success of the inversion procedure.

The transmission $\mathcal{T}_{j\ell}(E)$ is given by [55]

$$\mathcal{T}_{j\ell}(E) = \text{tr} [\mathbf{\Gamma}_\ell(E) \mathbf{G}^r(E) \mathbf{\Gamma}_j(E) \mathbf{G}^a(E)] \quad (3)$$

where $\mathbf{G}^r = (\mathbf{G}^a)^\dagger$ is the retarded Green's function of the full system, while $\mathbf{\Gamma}_\ell$ is the line or decay width matrix of the lead corresponding to the ℓ -terminal. Both \mathbf{G}^r and $\mathbf{\Gamma}_\ell$ are conveniently expressed in a discrete representation, typically a set of Wannier-like basis states. While \mathbf{G}^r has the dimension of the number of Wannier-like states in the central region, the dimension of $\mathbf{\Gamma}_\ell$ is the number of states at the ℓ -lead-central region interface. The leads are considered as semi-infinite and the decay widths are computed by the standard prescription [56]. Note that the most significant contribution to the integral in Eq. (2) comes from the transmission $\mathcal{T}_{j\ell}(E)$ at energies close to the chemical potential (Fermi level) μ . For that reason, throughout this manuscript we shall use the dimensionless energy-dependent transmission coefficient $\mathcal{T}_{j\ell}$ as a proxy for the conductance between electrodes j and ℓ .

The multi-terminal conductance expression, Eq. (2), is written in terms of Green functions and as such it is model independent. In other words, once the Hamiltonian is known one can find the corresponding Green function and subsequently obtain the energy dependent conductance of the system. The inversion method has been shown to work for single- [38] and multiple-orbital [52] tight-binding models, as well as for density functional theory calculations [38]. We stress that the method does not rely on any specific property of the electronic structure calculation implementation. For the sake of simplicity, we model the graphene electronic properties using a single-orbital nearest neighbour tight-binding Hamiltonian [51], namely $H = -t \sum_{\langle i,j \rangle} (c_i^\dagger c_j + \text{H.c.})$, where t is the hopping integral that we adopt as the energy unit and c_i^\dagger (c_i) stands for the operator of electron creation (annihilation) at the i th lattice site. The disorder is modeled by adding to the Hamiltonian H the local potential term $U = \lambda \sum_i c_i^\dagger c_i$, where i labels the randomly-selected impurity sites and $\lambda = t$ is the impurity on-site energy.

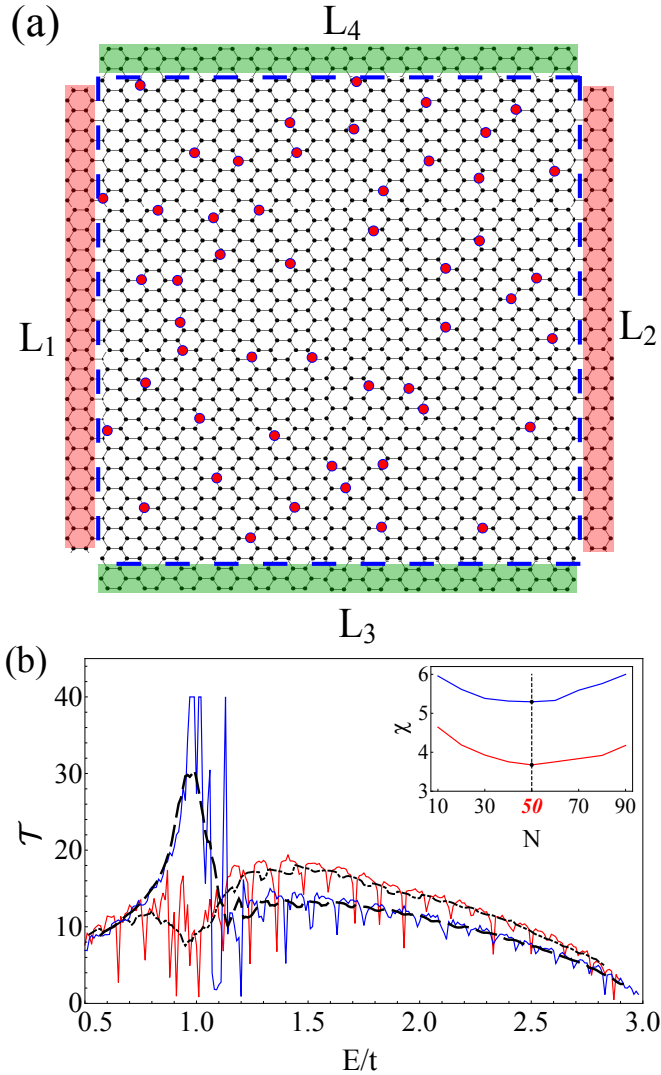


Figure 1. (a) Schematic representation of a graphene sheet contacted to multiple electrodes that span the entire device length. Vertical (horizontal) electrodes are labelled as L_1 and L_2 (L_3 and L_4). The device possesses a number of randomly distributed impurities represented by red dots. (b) Transmissions \mathcal{T}_{12} (blue) and \mathcal{T}_{34} (red) for a graphene sheet containing a total of 50 impurities, which translates into an overall concentration of $n = 1.5\%$, both plotted as a function of energy. Thick dashed lines represent the CA transmissions $\langle \mathcal{T}_{12} \rangle$ and $\langle \mathcal{T}_{34} \rangle$ for the same impurity concentration. The inset plots the concentration-dependent misfit functions $\chi_{12}(N)$ and $\chi_{34}(N)$.

Figure 1(b) shows the calculated values of \mathcal{T}_{12} and \mathcal{T}_{34} of a device of size $D_x = 25a$ and $D_y = 30\sqrt{3}a$, a being the lattice parameter of graphene, containing a total of $N = 50$ substitutional impurities, *i.e.* a concentration of $n = 1.5\%$, both plotted as a function of energy. The number of impurities N and its corresponding concentration n may be used interchangeably in the manuscript. Although the actual number of impurities and how they are spatially distributed in the parent Hamiltonian are

needed to generate \mathcal{T}_{12} and \mathcal{T}_{34} , this information is not to be used in any part of the subsequent calculations but serves only as a reference to be compared against the final inverted results. Therefore, the conductance is the sole input function for the inversion procedure. The transmissions \mathcal{T}_{12} and \mathcal{T}_{34} show fluctuations of order unit over small energy scales, consistent with the universal conductance fluctuation characteristic (chaotic) of ballistic and diffusive electronic transport [57, 58]. Hence, as previously alluded to, a naive approach attempting a comparison of the input function with the conductance for every single possible configuration is neither practical, since involves a prohibitively large number of combinations, nor insightful.

Fortunately, the inversion procedure introduced in [38] provides a far more efficient technique which combines Configuration-Average (CA) with the ergodic principle that associates average (energy) conductance of a single sample with sample-to-sample average at a fixed energy. More specifically, the ergodic hypothesis assumes that a running average over a continuous parameter upon which the conductance depends is equivalent to the ensemble average over different impurity configurations. In mathematical terms, this is done by considering the so-called misfit function defined as [38]

$$\chi_{jj'}(n) = \frac{1}{\mathcal{E}_+ - \mathcal{E}_-} \int_{\mathcal{E}_-}^{\mathcal{E}_+} dE [\mathcal{T}_{jj'}(E) - \langle \mathcal{T}_{jj'}(E) \rangle]^2, \quad (4)$$

where the integration limits \mathcal{E}_+ and \mathcal{E}_- are arbitrarily chosen energy values within the conduction band, provided $\mathcal{E}_+ - \mathcal{E}_-$ is much larger than the transmission autocorrelation width [38]. The CA transmission $\langle \mathcal{T}_{jj'} \rangle$ is defined as $\langle \mathcal{T}_{jj'} \rangle = (1/M) \sum_{m=1}^M \mathcal{T}_{jj'}^{(m)}$, where the superscript (m) labels the different realisations of disorder configurations. While both $\mathcal{T}_{jj'}$ and $\langle \mathcal{T}_{jj'} \rangle$ are functions of energy, the latter is also a function of impurity concentration n . When plotted as a function of n (or N), the misfit function is expected to display a minimum at a value that corresponds to the actual impurity concentration.

This can be seen in the inset of Fig. 1(b) where the misfit functions χ_{12} and χ_{34} are plotted as a function of the impurity number N . Both curves are obviously different but, reassuringly, display distinctive minima at the same concentration value of $N = 50$, which coincides exactly with the chosen impurity concentration that generates the transmission matrix elements \mathcal{T}_{ij} . Furthermore, when plotting the CA transmissions $\langle \mathcal{T}_{12} \rangle$ and $\langle \mathcal{T}_{34} \rangle$ evaluated for the same impurity concentration we find very good agreement with the input functions \mathcal{T}_{12} and \mathcal{T}_{34} , as seen in Fig. 1(b). This is unmistakable evidence that the inversion method introduced in [38] can indeed account for the case of multiple electrodes.

One question that may arise at this point is about the computational cost of calculating the misfit function since it contains an energy integral as well as an aver-

age involving M configurations of disorder, not to mention the need to repeat the same procedure for a range of concentration values. Firstly, although expressed as an integral, the misfit function can be calculated as a discrete sum containing a reasonably small number of terms, usually 50 or more, without compromising in accuracy. Regarding the CA procedure, we find that by taking $M \gtrsim 10^3$ configurations leads to results for the inverted concentrations with errors well below 5%, a remarkable achievement for a quantum inversion procedure [38]. Finally, regarding the need to evaluate the misfit function for several concentration values, we adopt a machine-learning-based interpolating scheme [52] that provides excellent resolution in $\chi_{1,2}(n)$ generated with only 5 distinct concentration values.

Instead of using conductance readings between full-length electrode pairs that provide information about the overall impurity concentration, we may also interrogate the system with any pair of electrodes that do not necessarily span the entire device. Let us then consider the conductance $\mathcal{T}_{\tilde{1},\tilde{2}}(E)$ of the same device but this time current is being injected from the bottom left half-length electrode and extracted from its mirror-image electrode on the right, as shown in Fig. 2(a). Vertical and horizontal dashed lines are drawn as a guide to the eyes in order to separate the impurities into four distinct cells. With the intention of resolving the impurity number in each of these cells, we label them N_1 to N_4 , as indicated in Fig. 2(a). For the sake of differentiation to the case of full-length electrodes, we use the symbol \sim placed above the electrode-label integer to indicate that only a fraction of its length is active for current injection and extraction. In this case, the integers \tilde{j} represent electrodes with only half of their full length in contact with the conductor. Similar steps can be taken in regard to the CA conductances in order to obtain the misfit functions defined in Eq.(4) but this time the impurity numbers within the device may be broken into two separate parts: $N_T = N_1 + N_2$ and $N_B = N_3 + N_4$, i.e., the top- and bottom-half values, respectively. This apparently adds one extra degree of freedom to the misfit function which should now read $\chi_{\tilde{1},\tilde{2}}(N_T, N_B)$. Finding the minimum of $\chi_{\tilde{1},\tilde{2}}(N_T, N_B)$ would in principle involve searching for minima of a two-variable function, but thanks to the previously obtained information about the total number of impurities in the device, we know that both variables are not independent but constrained to obey $N_T + N_B = N$. This is thus equivalent to a single-variable search and is similar to the one shown in Fig. 1.

In addition, the same can be done with horizontally placed electrodes. In this case $\mathcal{T}_{\tilde{3},\tilde{4}}$ corresponds to the conductance between the top and bottom half-length electrodes on the left of the device. Once again, two new variables are defined, namely, $N_L = N_1 + N_3$ and $N_R = N_2 + N_4$, which are the impurity numbers on the left and right halves of the device, respectively. The mis-

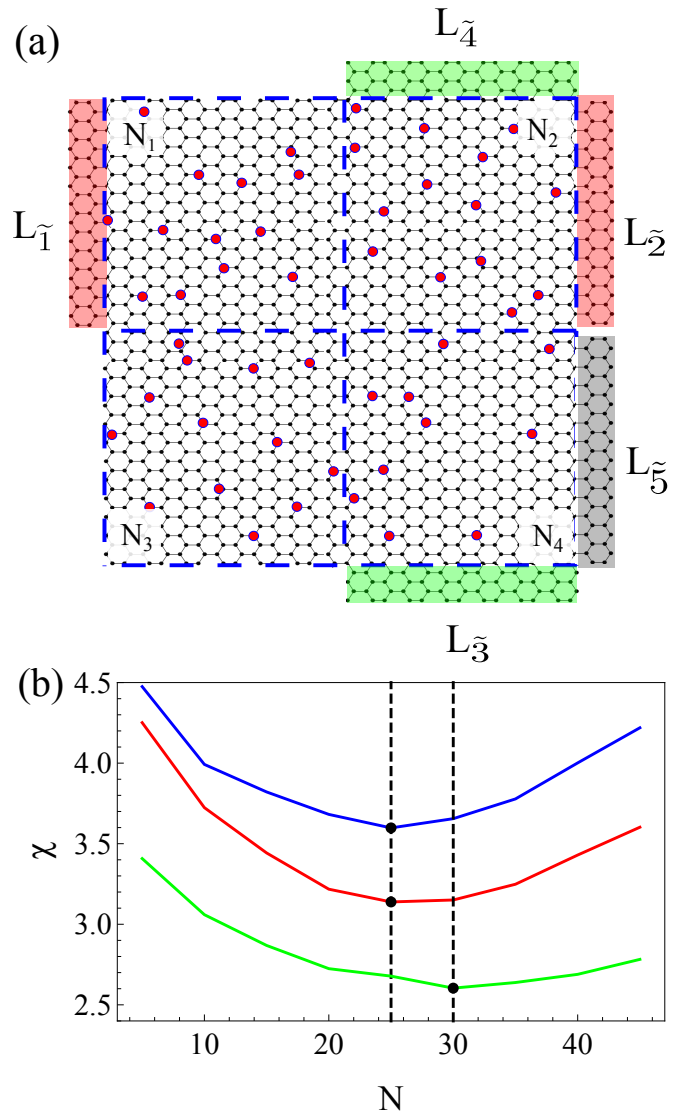


Figure 2. (a) Schematic representation of the same graphene sheet of Fig. 1 with electrodes now spanning half of the device length. The system is divided into four cells, all delineated by blue dashed lines. N_j corresponds to the number of impurities in the j th cell. (b) Misfit functions $\chi_{\tilde{1},\tilde{2}}$ (red), $\chi_{\tilde{3},\tilde{4}}$ (green), and $\chi_{\tilde{1},\tilde{5}}$ (blue) plotted as a function of the number of impurities in. Vertical dashed lines indicate the distinctive minima of the misfit functions.

fit function $\chi_{\tilde{3},\tilde{4}}(N_L, N_R)$ that results from Eq. (4) is another two-variable function that in practice depends only on one of them because they are also constrained to satisfy $N_L + N_R = N$. Fig. 2(b) depicts the corresponding misfit functions $\chi_{\tilde{1},\tilde{2}}$ plotted as a function of N_T and $\chi_{\tilde{3},\tilde{4}}$ plotted as a function of N_L . Both curves display clearly distinctive minima located at values $N_T = 30$ and $N_L = 25$, respectively, which coincide exactly with the numbers seen in the cells of Fig. 2(a). Combined with the previously obtained result of $N = 50$, in this case we may conclude that $N_B = 25$ and $N_R = 25$. Knowing

N_T , N_B , N_L and N_R is not sufficient to uniquely identify the impurity numbers in each one of the four cells. For that an additional inversion involving the conductance between diagonally opposite electrodes is required, which is achieved with $\mathcal{T}_{\tilde{1},\tilde{5}}$. A similar procedure leads to the corresponding misfit function $\chi_{\tilde{1},\tilde{5}}(N_D, N_{D'})$, where the variables $N_D = N_1 + N_4$ and $N_{D'} = N_2 + N_3$ refer to the impurity numbers along the two diagonals. Obviously, they must also obey that $N_D + N_{D'} = N$. Fig. 2(b) also shows $\chi_{\tilde{1},\tilde{5}}$ plotted as a function of N_D , with a clear minimum at $N_D = 25$. The set of equations that cast these constraints is easily solved when expressed in matrix form, *i.e.*,

$$\begin{pmatrix} N_1 \\ N_2 \\ N_3 \\ N_4 \end{pmatrix} = \begin{pmatrix} 1 & 1 & 0 & 0 \\ 1 & 0 & 1 & 0 \\ 0 & 0 & 1 & 1 \\ 1 & 0 & 0 & 1 \end{pmatrix}^{-1} \begin{pmatrix} N_T \\ N_L \\ N_B \\ N_D \end{pmatrix}, \quad (5)$$

which leads to the impurity numbers on each of the four cells. In this case, $N_1 = 10$, $N_2 = 15$, $N_3 = 15$ and $N_4 = 10$. Remarkably, this is somewhat analogous to solving a Sudoku puzzle that starts from the conductance readings and finds the exact impurity numbers within each cell by imposing that they must add up to the specific values (N_T , N_L , N_B and N_D) which are themselves determined through our inversion procedure.

Since by interrogating the disordered device with half-length electrodes we were able to spatially resolve the impurity concentration into four quarters, readings with even shorter electrodes are likely to improve the spatial resolution. In fact, the same Sudoku-style procedure can be carried out starting from conductance readings of $\mathcal{T}_{\tilde{i},\tilde{j}}$ where now the symbol \approx above the integers in question are used to indicate that only one quarter of the i and j electrodes are active, as seen in Fig. 3. Dashed lines in panels (a) and (b) are used to delineate nine and sixteen cells, respectively, each containing a certain fraction of the total number of impurities. Double-sided arrows represent the quarter-length electrodes and the underlying hexagonal atomic structure has been omitted to avoid too congested a figure. Our goal is to find the exact impurity number (concentration) in each one of these cells and the procedure is analogous to the case of four cells. The difference lies primarily in how the cells are clustered when carrying out the inversion. While the results of Fig. 2 were obtained by combining cells into rows and columns, there are very many ways of selecting how the individual cells can be clustered. This gives an enormous degree of flexibility on finding the actual number of impurities in each cell. Examples of a few different ways in which this is done can be found in the Supplemental Material (SM). For the sake of comparison, the boldface integers on the left and right parts of Table I indicate the impurity number N_j in cell j found through the Sudoku-style inversion in the case of nine and sixteen cells, respectively. Also

7 (6)	8 (7)	5 (6)	0 (2)	2 (3)	5 (4)	3 (4)
8 (7)	5 (4)	7 (6)	7 (5)	4 (3)	1 (2)	3 (3)
4 (5)	5 (6)	3 (3)	5 (5)	2 (3)	6 (4)	2 (2)

3 (2)	2 (3)	3 (3)	2 (2)
--------------	--------------	--------------	--------------

Table I. Boldface integers indicate the number of impurities obtained from the Sudoku-style inversion. The accompanying integers in parenthesis indicate the real number as per Fig. 3. Left: 3 x 3; Right: 4 x 4

shown in parenthesis is the real number of impurities contained in each cell. Note that the agreement is very good and that discrepancies rarely exceed a single unit. It is worth mentioning that natural uncertainties arise when impurities lie very close to the dashed lines separating the cells, since their scattering range may extend over more than one cell. This is particularly problematic as the cells are made smaller and the ratio between the cell perimeter and its area increases.

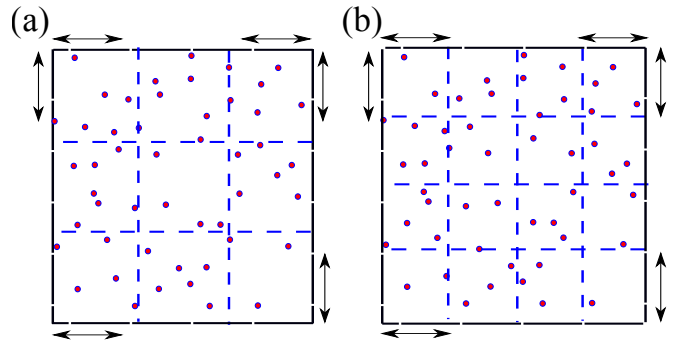


Figure 3. A schematic representation of the device with quarter-length electrodes (see main text for a precise definition) represented by double-sided arrows. The dashed lines are used simply to delineate the cells in the case of (a) nine cells; (b) sixteen cells.

To demonstrate that there is great flexibility in how the device can be interrogated, we reproduce one of the cases shown previously and resolve the impurity concentration into four quadrants but this time we adopt a couple of different setups for the electrodes, as shown in the SM. In one case the injecting and extracting electrodes are not of similar sizes, with one being full-length and the other quarter-length. In the other case, four point-like electrodes are placed on the corners of the device. Both settings render the same findings as the ones shown in Fig. 2. That degree of flexibility suggests that a wide range of different possibilities exists to probe the local conductances of disordered 2D materials in order to map how their impurities and defects are spatially distributed.

Regarding the achieved success rate, we test the inversion accuracy by defining the error as $\alpha = \frac{1}{J} \sum_j^J |N_j^{\min} - N_j^P| / N_j^P$, where N_j^P is the number of impurities in cell j of the parent (input) configuration and N_j^{\min} is the corresponding value that minimizes the misfit function.

α consists of an average over the total number of cells J , so that large values of J correspond to higher spatial resolution in the impurity distribution. Having considered the cases of $J = 1$, $J = 4$, $J = 9$ and $J = 16$, we may conclude that the inversion accuracy decreases as we attempt to increase the resolution, as seen in Table II. These values are obtained out of repeated inversions from 100 different parent configurations in order to achieve statistical significance. Given the diverse ways in which a device can be probed and interrogated, it is possible that by increasing the number of readings and/or by selecting more appropriate electrode setups, the accuracy can be further improved. Remarkably, moderate resolution can be achieved in mapping how impurities are distributed with this inversion methodology.

Finally, the Sudoku-style inversion tool presented here has been based entirely on multi-terminal conductance measurements serving as input functions. However, the basic non-spatially-resolving inversion has been shown to work with other input signals[38, 52]. In fact, other quantities that can be written in terms of two-point correlation functions are very likely candidates to display similar characteristics in the presence of disorder and, therefore, may serve as potential input functions from which spatial mapping of impurity concentration becomes possible. This may pave the way to using thermal conductivities, spin susceptibilities, to name but a few, as sources capable of providing spatial information about a disordered device when only moderate resolution is required.

In summary, we have shown how a recently proposed inversion methodology capable of identifying the global number of impurities from seemingly noisy two-terminal conductance signals of a 2D quantum device can be extended to determine how such impurities are spatially distributed. By generalising the method to a multi-terminal framework and mapping the device into a grid-like structure, the inversion specifies the total impurity number in separate rows and columns. These are constraints that must be satisfied in order to find the exact concentration in each one of the individual cells, in a way that resembles a Sudoku puzzle. The impurity distribution can be resolved into smaller sections of the device, depending on how the local conductance is being probed and on the dimensions of the probing electrodes. Furthermore, spatial resolution can certainly be improved by increasing the number of conductance readings. We envisage this inversion methodology being implemented beyond conductance measurements which will provide a framework for visualising impurities from simple measurements of different physical properties.

ACKNOWLEDGMENTS

This publication has emanated from research supported in part by a research grant from Sci-

# of cells J	accuracy α
1	0.037
4	0.12
9	0.17
16	0.21

Table II. Inversion method accuracy α for different number of cells J .

ence Foundation Ireland (SFI) under Grant Number SFI/12/RC/2278-P2. C.L acknowledges financial support from CNPq under Grant #313059/2020-9 and from FAPERJ under Grant #E-26/202.882/2018.

- [1] M. Bertero and M. Piana, Inverse problems in biomedical imaging: modeling and methods of solution, in *Complex Systems in Biomedicine*, edited by A. Quarteroni, L. Formaggia, and A. Veneziani (Springer Milan, Milano, 2006) pp. 1–33.
- [2] J. Virieux, A. Asnaashari, R. Brossier, L. Métivier, A. Ribodetti, and W. Zhou, An introduction to full waveform inversion, in *Encyclopedia of Exploration Geophysics* (2017) pp. R1–1–R1–40.
- [3] J. Tromp, D. Komatitsch, and Q. Liu, Spectral-element and adjoint methods in seismology, *Communications in Computational Physics* **3**, 1 (2008).
- [4] E. T. F. Dias and H. Vieira Neto, A novel approach to environment mapping using sonar sensors and inverse problems, in *Towards Autonomous Robotic Systems*, edited by C. Dixon and K. Tuyls (Springer International Publishing, Cham, 2015) pp. 100–111.
- [5] M. Lassas, L. Päiväranta, and E. Saksman, Inverse scattering problem for a two dimensional random potential, *Commun. Math. Phys.* **279**, 669 (2008).
- [6] T. M. Hoang, C. S. Gerving, B. J. Land, M. Anquez, C. D. Hamley, and M. S. Chapman, Dynamic stabilization of a quantum many-body spin system, *Phys. Rev. Lett.* **111**, 090403 (2013).
- [7] E. Chertkov and B. K. Clark, Computational inverse method for constructing spaces of quantum models from wave functions, *Phys. Rev. X* **8**, 031029 (2018).
- [8] R.-Y. Lai, R. Shankar, D. Spirn, and G. Uhlmann, An inverse problem from condensed matter physics, *Inverse Problems* **33**, 115011 (2017).
- [9] E. Tsymbal and P. Dowben, Grand challenges in condensed matter physics: from knowledge to innovation, *Frontiers in Physics* **1**, 32 (2013).
- [10] J. van der Gucht, Grand challenges in soft matter physics, *Frontiers in Physics* **6**, 87 (2018).
- [11] G. Bertaina, D. E. Galli, and E. Vitali, Statistical and computational intelligence approach to analytic continuation in Quantum Monte Carlo, *Advances in Physics: X* **2**, 302 (2017).
- [12] A. Franceschetti and A. Zunger, The inverse band-structure problem of finding an atomic configuration with given electronic properties, *Nature* **402**, 60 (1999).
- [13] L. Yu, R. S. Kokenyesi, D. A. Keszler, and A. Zunger, Inverse design of high absorption thin-film photovoltaic materials, *Adv. Energy Mater.* **3**, 43 (2013).

[14] M. F. Kasim, T. Galligan, J. T. Mugglestone, G. Gregori, and S. M. Vinko, Inverse problem instabilities in large-scale modelling of matter in extreme conditions, *Phys. Plasmas* **26**, 112706 (2019).

[15] D. S. Jensen and A. Wasserman, Numerical methods for the inverse problem of density functional theory, *Int. J. Quantum Chem.* **118**, e25425 (2018).

[16] R. Fournier, L. Wang, O. V. Yazyev, and Q. Wu, Artificial neural network approach to the analytic continuation problem, *Phys. Rev. Lett.* **124**, 056401 (2020).

[17] L. Zhang, J.-W. Luo, A. Saraiva, B. Koiller, and A. Zunger, Genetic design of enhanced valley splitting towards a spin qubit in silicon, *Nat. Commun.* **4**, 2396 (2013).

[18] R. A. Vargas-Hernández, Y. Guan, D. H. Zhang, and R. V. Krems, Bayesian optimization for the inverse scattering problem in quantum reaction dynamics, *New J. Phys.* **21**, 022001 (2019).

[19] O. Kyriienko, Quantum inverse iteration algorithm for programmable quantum simulators, *npj Quantum Information* **6** (2020).

[20] A. Lopez-Bezanilla and O. A. von Lilienfeld, Modeling electronic quantum transport with machine learning, *Phys. Rev. B* **89**, 235411 (2014).

[21] K. Hansen, G. Montavon, F. Biegler, S. Fazli, M. Rupp, M. Scheffler, O. A. von Lilienfeld, A. Tkatchenko, and K.-R. Müller, Assessment and validation of machine learning methods for predicting molecular atomization energies, *J. Chem. Theory Comput.* **9**, 3404 (2013).

[22] B. Himmeloglu, Tree based machine learning framework for predicting ground state energies of molecules, *J. Chem. Phys.* **145**, 134101 (2016).

[23] H. Li, C. Collins, M. Tanha, G. J. Gordon, and D. J. Yaron, A density functional tight binding layer for deep learning of chemical Hamiltonians, *J. Chem. Theory Comput.* **14**, 5764 (2018).

[24] R. Xia and S. Kais, Quantum machine learning for electronic structure calculations, *Nat. Commun.* **9**, 4195 (2018).

[25] P. O. Dral, Quantum chemistry in the age of machine learning, *J. Phys. Chem. Lett.* **11**, 2336 (2020).

[26] J. Carrasquilla and R. G. Melko, Machine learning phases of matter, *Nat. Phys.* **13**, 431 (2017).

[27] G. R. Schleder, A. C. M. Padilha, C. M. Acosta, M. Costa, and A. Fazzio, From DFT to machine learning: recent approaches to materials science-a review, *Journal of Physics: Materials* **2**, 032001 (2019).

[28] A. Ziletti, D. Kumar, M. Scheffler, and L. M. Ghiringhelli, Insightful classification of crystal structures using deep learning, *Nat. Commun.* **9**, 2775 (2018).

[29] R. Potyrailo, K. Rajan, K. Stoewe, I. Takeuchi, B. Chisholm, and H. Lam, Combinatorial and high-throughput screening of materials libraries: Review of state of the art, *ACS Comb. Sci.* **13**, 579 (2011).

[30] S. K. Suram, P. F. Newhouse, L. Zhou, D. G. Van Campen, A. Mehta, and J. M. Gregoire, High throughput light absorber discovery, part 2: Establishing structure-band gap energy relationships, *ACS Comb. Sci.* **18**, 682 (2016).

[31] H. Koinuma and I. Takeuchi, Combinatorial solid-state chemistry of inorganic materials, *Nat. Mater.* **3**, 429 (2004).

[32] M. L. Green, C. L. Choi, J. R. Hattrick-Simpers, A. M. Joshi, I. Takeuchi, S. C. Barron, E. Campo, T. Chiang, S. Empedocles, J. M. Gregoire, A. G. Kusne, J. Martin, A. Mehta, K. Persson, Z. Trautt, J. Van Duren, and A. Zakutayev, Fulfilling the promise of the materials genome initiative with high-throughput experimental methodologies, *Appl. Phys. Rev.* **4**, 011105 (2017).

[33] S. Curtarolo, G. L. W. Hart, M. B. Nardelli, N. Mingo, S. Sanvito, and O. Levy, The high-throughput highway to computational materials design, *Nat. Mater.* **12**, 191 (2013).

[34] L. Yu and A. Zunger, Identification of potential photovoltaic absorbers based on first-principles spectroscopic screening of materials, *Phys. Rev. Lett.* **108**, 068701 (2012).

[35] C. C. Fischer, K. J. Tibbets, D. Morgan, and G. Ceder, Predicting crystal structure by merging data mining with quantum mechanics, *Nat. Mater.* **5**, 641 (2006).

[36] R. Gautier, X. Zhang, L. Hu, L. Yu, Y. Lin, T. O. L. Sunde, D. Chon, K. R. Poeppelmeier, and A. Zunger, Prediction and accelerated laboratory discovery of previously unknown 18-electron abx compounds, *Nat. Chem.* **7**, 308 (2015).

[37] J. Schmidt, M. R. G. Marques, S. Botti, and M. A. L. Marques, Recent advances and applications of machine learning in solid-state materials science, *npj Computational Materials* **5**, 83 (2019).

[38] S. Mukim, F. P. Amorim, A. R. Rocha, R. B. Muniz, C. Lewenkopf, and M. S. Ferreira, Disorder information from conductance: A quantum inverse problem, *Phys. Rev. B* **102**, 075409 (2020).

[39] F. Ghahari, Y. Zhao, P. Cadden-Zimansky, K. Bolotin, and P. Kim, Measurement of the $\nu = 1/3$ fractional quantum hall energy gap in suspended graphene, *Phys. Rev. Lett.* **106**, 046801 (2011).

[40] X. Cui, G.-H. Lee, Y. D. Kim, G. Arefe, P. Y. Huang, C.-H. Lee, D. A. Chenet, X. Zhang, L. Wang, F. Ye, F. Pizzocchero, B. S. Jessen, K. Watanabe, T. Taniguchi, D. A. Muller, T. Low, P. Kim, and J. Hone, Multi-terminal transport measurements of MoS₂ using a van der waals heterostructure device platform, *Nature Nanotechnology* **10**, 534 (2015).

[41] T. Ihn, *Semiconductor Nanostructures* (Oxford University Press, Oxford, 2010).

[42] M. Büttiker, Four-terminal phase-coherent conductance, *Phys. Rev. Lett.* **57**, 1761 (1986).

[43] M. Jura, M. Topinka, L. Urban, A. Yazdani, H. Shtrikman, L. N. Pfeiffer, K. W. West, and D. Goldhaber-Gordon, Unexpected features of branched flow through high-mobility two-dimensional electron gases, *Nat. Phys.* **3**, 841–845 (2007).

[44] B. A. Braem, F. M. D. Pellegrino, A. Principi, M. Röösli, C. Gold, S. Hennel, J. V. Koski, M. Berl, W. Dietsche, W. Wegscheider, M. Polini, T. Ihn, and K. Ensslin, Scanning gate microscopy in a viscous electron fluid, *Phys. Rev. B* **98**, 241304 (2018).

[45] B. Brun, N. Moreau, S. Somanchi, V.-H. Nguyen, K. Watanabe, T. Taniguchi, J.-C. Charlier, C. Stampfer, and B. Hackens, Imaging Dirac fermions flow through a circular Veselago lens, *Phys. Rev. B* **100**, 041401 (2019).

[46] B. Brun, N. Moreau, S. Somanchi, V.-H. Nguyen, A. Mrećica-Kolasińska, K. Watanabe, T. Taniguchi, J.-C. Charlier, C. Stampfer, and B. Hackens, Optimizing Dirac fermions quasi-confinement by potential smoothness engineering, *2D Materials* **7**, 025037 (2020).

- [47] A.-P. Li, K. W. Clark, X.-G. Zhang, and A. P. Baddorf, Electron transport at the nanometer-scale spatially revealed by four-probe scanning tunneling microscopy, *Advanced Functional Materials* **23**, 2509 (2013).
- [48] J. Baringhaus, M. Ruan, F. Edler, A. Tejeda, M. Sicot, A. Taleb-Ibrahimi, A.-P. Li, Z. Jiang, E. H. Conrad, C. Berger, C. Tegenkamp, and W. A. de Heer, Exceptional ballistic transport in epitaxial graphene nanoribbons, *Nature* **506**, 349 (2014).
- [49] J. Duffy, J. Lawlor, C. Lewenkopf, and M. S. Ferreira, Impurity invisibility in graphene: Symmetry guidelines for the design of efficient sensors, *Phys. Rev. B* **94**, 045417 (2016).
- [50] E. Ridolfi, L. R. F. Lima, E. R. Mucciolo, and C. H. Lewenkopf, Electronic transport in disordered MoS₂ nanoribbons, *Phys. Rev. B* **95**, 035430 (2017).
- [51] A. H. Castro Neto, F. Guinea, N. M. R. Peres, K. S. Novoselov, and A. K. Geim, The electronic properties of graphene, *Rev. Mod. Phys.* **81**, 109 (2009).
- [52] F. R. Duarte Filho, S. Mukim, A. Molina Sanchez, T. Rappoport, and M. S. Ferreira, Decoding the DC and optical conductivities of disordered MoS₂ films: an inverse problem, *New Journal of Physics* (2021).
- [53] L. R. F. Lima, A. Dusko, and C. Lewenkopf, Efficient method for computing the electronic transport properties of a multiterminal system, *Phys. Rev. B* **97**, 165405 (2018).
- [54] L. R. F. Lima and C. Lewenkopf, Local equilibrium charge and spin currents in two-dimensional topological systems (2021), [arXiv:2104.07206 \[cond-mat.mes-hall\]](https://arxiv.org/abs/2104.07206).
- [55] Y. Meir and N. S. Wingreen, Landauer formula for the current through an interacting electron region, *Phys. Rev. Lett.* **68**, 2512 (1992).
- [56] C. H. Lewenkopf and E. R. Mucciolo, The recursive Green's function method for graphene, *J. Comput. Electron.* **12**, 203 (2013).
- [57] P. A. Lee and A. D. Stone, Universal conductance fluctuations in metals, *Phys. Rev. Lett.* **55**, 1622 (1985).
- [58] C. W. J. Beenakker, Random-matrix theory of quantum transport, *Rev. Mod. Phys.* **69**, 731 (1997).

Spatial mapping of disordered 2D materials: the conductance Sudoku

S. Mukim,¹ C. Lewenkopf,² and M. S. Ferreira^{1,3}

¹*School of Physics, Trinity College Dublin, Dublin 2, Ireland*

²*Instituto de Física, Universidade Federal Fluminense, 24210-346 Niterói, Brazil*

³*Centre for Research on Adaptive Nanostructures and Nanodevices (CRANN) & Advanced Materials and Bioengineering Research (AMBER) Centre, Trinity College Dublin, Dublin 2, Ireland*

(Dated: February 28, 2022)

Flexibility of the inversion procedure allows more than one approach to extract spatial information of the disordered components inside the flake. In the main manuscript the graphene flake is resolved into four quarters making use of half-length electrodes. Using shorter electrodes, it is possible to resolve the impurity distribution into a larger number of smaller cells. Figs. 1 and 2 show a schematic representation of the graphene flake connected with six quarter-length electrodes, together with imaginary dashed (blue) lines resolving the graphene flake into 9 and 16 cells, respectively. We defined a system of four linear equations in the main manuscript to resolve the flake in quarter cells. To resolve it in 9 or 16 cells we need to define a system of linear equations which can be written in the form

$$AX - B = \lambda, \quad (1)$$

where A is a square matrix and the other elements are all single-column vectors whose size matches the number of cells. For example, in the case of 9 cells the equation takes the form of Eq. (1) with $\lambda = 0$. Matrix A contains information about regions chosen to define 9 misfit functions such that $\det A \neq 0$. Variables N_i , with i running from 1 to 9, indicate the impurity occupation of the individual cells shown in Fig. 2 and M_i is the occupation of corresponding region obtained from the inversion. Note that we have flexibility on how we choose to interrogate the different parts of the flake, which means that the form of matrix A is not unique but depends on that exact choice. Eq. 2 shows one such choice of a system of linear equations for the given arrangement of electrodes.

$$\begin{pmatrix} 1 & 1 & 1 & 0 & 0 & 0 & 0 & 0 & 0 \\ 0 & 0 & 0 & 1 & 1 & 1 & 0 & 0 & 0 \\ 1 & 1 & 1 & 1 & 1 & 1 & 1 & 1 & 1 \\ 1 & 0 & 0 & 1 & 0 & 0 & 1 & 0 & 0 \\ 0 & 1 & 0 & 0 & 1 & 0 & 0 & 1 & 0 \\ 1 & 1 & 0 & 1 & 1 & 0 & 0 & 0 & 1 \\ 1 & 0 & 0 & 1 & 0 & 0 & 0 & 1 & 1 \\ 1 & 0 & 0 & 0 & 1 & 1 & 0 & 1 & 1 \\ 1 & 1 & 0 & 0 & 0 & 1 & 0 & 0 & 1 \end{pmatrix} \cdot \begin{pmatrix} N_1 \\ N_2 \\ N_3 \\ N_4 \\ N_5 \\ N_6 \\ N_7 \\ N_8 \\ N_9 \end{pmatrix} = \begin{pmatrix} M_1 \\ M_2 \\ M_3 \\ M_4 \\ M_5 \\ M_6 \\ M_7 \\ M_8 \\ M_9 \end{pmatrix} \quad (2)$$

For example, the top-row identity from the matrix equation above reads that $N_1 + N_2 + N_3 = M_1$. By minimising a misfit function defined in terms of the variable M_1 , we obtain the exact number of impurities in the top row of

the flake, as shown in Fig. 1. The same must be done with other regions such that we find the values of all M_i in Eq.(2). Analogously to the four-cell case, the inversion is carried out with a few different readings. In this case, M_1 , M_2 and M_3 are found from $\mathcal{T}_{\tilde{1},\tilde{2}}$; M_4 , M_5 and M_6 are found from $\mathcal{T}_{\tilde{4},\tilde{6}}$; M_7 and M_8 are found from $\mathcal{T}_{\tilde{1},\tilde{3}}$; finally M_9 is obtained from $\mathcal{T}_{\tilde{4},\tilde{5}}$.

The remaining task is to solve the sudoku-style puzzle of identifying the impurity numbers N_i of individual cells constrained to match the values of M_i . We obviously must account for the possibility of error in the inversion procedure which would lead to the incorrect mapping of the disorder concentration. This can be alleviated by obtaining more information about the flake and availing of more misfit functions, which will then serve as extra constraints in Eq.(1). Constrained optimization methods like Lagrange multiplier or differential evolution are very well established procedures and are suitable to be used here to find the values of N_j .

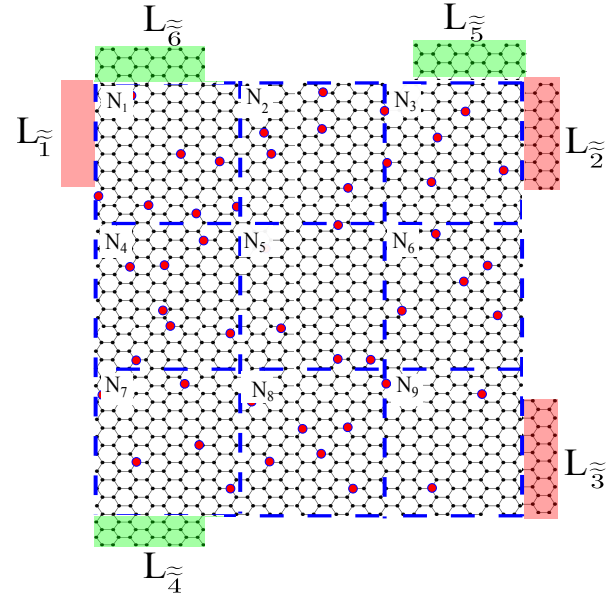


FIG. 1. A schematic representation of graphene flake embedded with substitutional disorders. Electrodes labelled as L_i i running from 1 to 6 are of quarter length of the flake size. Dashed lines defined the flake in 9 different regions labelled as N_1 to N_9 .

Left half of Table I in the main manuscript displays the

numbers found for the nine cells together with the real occupation (in brackets). The agreement between the numbers is very good and the discrepancy is not more than a single impurity.

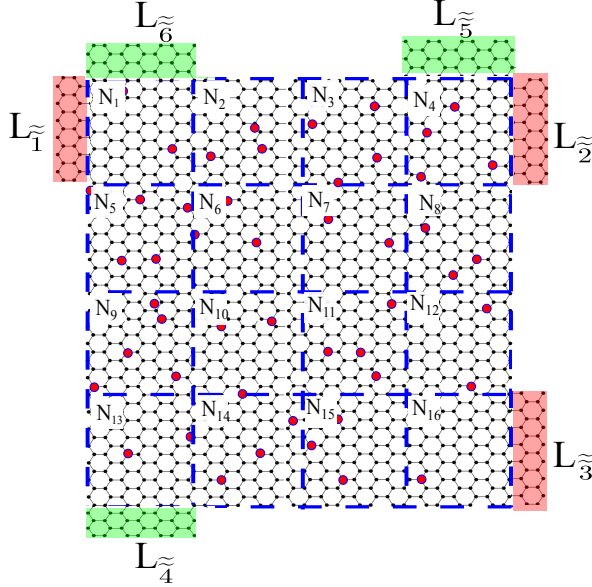


FIG. 2. A schematic representation of graphene flake embedded with substitutional disorders. Electrodes labelled as L_i running from 1 to 6 are of quarter length of the flake size. Dashed lines defined the flake in 16 different regions labelled as N_1 to N_{16} .

In the case of sixteen cells, the dashed lines of Fig. 2 delineate them together with the corresponding occupation numbers N_i , with i running from 1 to 16. Analogously to the previous cases considered and in line with Eq.(1), we must select regions based on which the misfit function will be calculated. In the case of four quarters in the main manuscript, $\mathcal{T}_{\tilde{1},\tilde{2}}$ served as input to the misfit function in order to extract information about top half of the flake. For the quarter-length electrode arrangement, the same method can be implemented to obtain occupation of each of the four rows. We define such misfit function as $\chi_{\tilde{1},\tilde{2}}(N_a, N_b, N_c, N_d)$ where N_a is the occupation of disorders in the first row, N_b second row and so on as shown in Fig. 3(a) with blue, black and red lines contouring respective area of the flake. Note that occupation in rows is constrained by $N_a + N_b + N_c + N_d = N_{\text{total}}$.

Similarly, misfit function defined using the input in form of $\mathcal{T}_{\tilde{4},\tilde{5}}$ yields total occupation (N_e, N_f, N_g , and N_h) in each column of the flake in Fig. 2. The remaining equations needed to complete the system of linear equations come from the diagonal misfit functions. Diagonal misfit functions are defined using input transmission spectra from leads which are diagonally opposite to each other, namely $L_{\tilde{1},\tilde{3}}$ and $L_{\tilde{4},\tilde{5}}$. We need to define a system of sixteen linear equations to obtain the occupation

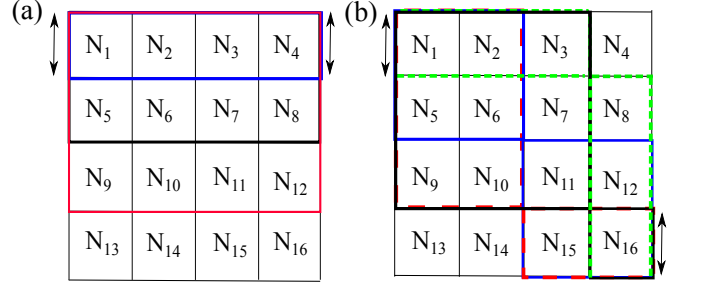


FIG. 3. Flake is resolved into 16 cells with N_i running from 1 to 16 gives occupation of each cell of the flake. (a) Misfit function and corresponding CA is defined for the regions enclosed in blue, black and red lines for input signal generated from leads position presented in the form of double arrow lines. (b) For the leads positioned diagonally opposite of the flake dashed red green lines shows non-trivial consideration of region for the inversion.

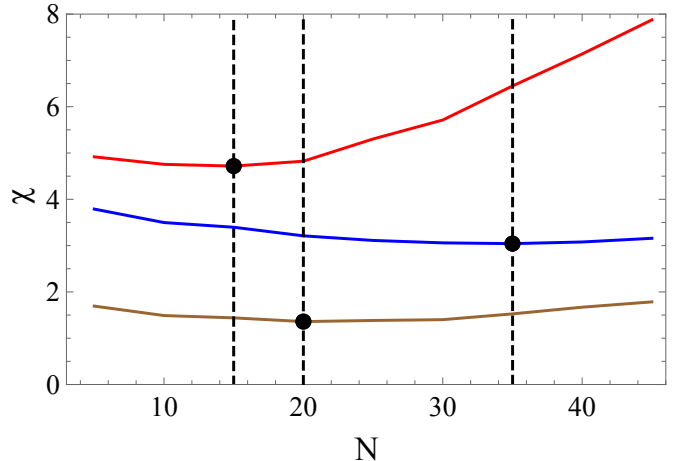


FIG. 4. Misfit function in blue defined for region enclosed in the thick black line in Fig. 3(b) shows minimum at $N = 35$ which closely coincides with $N = 37$ actual number of disorders in region. Brown and red misfit curves locates the occupation of regions enclosed by dashed red line and dashed green line of Fig. 3.

of each one of the cells. We have seven equations coming from $L_{\tilde{1},\tilde{3}}$ and $L_{\tilde{4},\tilde{5}}$. Two extra input signals from diagonally arranged leads will provide the remaining equations, namely $\mathcal{T}_{\tilde{1},\tilde{3}}$ and $\mathcal{T}_{\tilde{4},\tilde{5}}$. Using $\mathcal{T}_{\tilde{1},\tilde{3}}$ as input the flake is scanned in four different regions as shown in Fig. 3 contoured by dashed lines in black, green, red and blue colours.

In Fig. 4, three misfit functions are plotted as a function of number of impurities. Misfit function in red is defined with variables enclosed by dashed red line shown in Fig. 3(b). Misfit function in blue is defined for region enclosed by black lines in the schematic representation seen in Fig. 3(b). It is worth mentioning that the misfit function is minimum at $N = 35$ and when compared with the actual distribution of impurities in the parent config-

uration the discrepancy does not exceed two impurities. Finally, the misfit function defined using the input signal $\mathcal{T}_{\tilde{4},\tilde{5}}$ completes the set of equations necessary to generate the system of linear equations. It is important to note that this is by no means the only way to resolve the device in sixteen cells. Different arrangement of leads may lead to different ways of mapping the impurities. Following our definition and choice for how the system was probed, the matrix A of Eq.(1) is given by

$$A = \begin{pmatrix} 1 & 1 & 1 & 1 & 0 & 0 & 0 & 0 & 0 & 0 & 0 & 0 & 0 & 0 & 0 & 0 \\ 0 & 0 & 0 & 0 & 1 & 1 & 1 & 1 & 0 & 0 & 0 & 0 & 0 & 0 & 0 & 0 \\ 0 & 0 & 0 & 0 & 0 & 0 & 0 & 0 & 0 & 1 & 1 & 1 & 1 & 0 & 0 & 0 \\ 0 & 0 & 0 & 0 & 0 & 0 & 0 & 0 & 0 & 0 & 0 & 0 & 0 & 1 & 1 & 1 \\ 1 & 0 & 0 & 0 & 1 & 0 & 0 & 0 & 1 & 0 & 0 & 0 & 1 & 0 & 0 & 0 \\ 0 & 1 & 0 & 0 & 0 & 1 & 0 & 0 & 0 & 1 & 0 & 0 & 0 & 1 & 0 & 0 \\ 0 & 0 & 1 & 0 & 0 & 0 & 1 & 0 & 0 & 0 & 1 & 0 & 0 & 0 & 1 & 0 \\ 1 & 1 & 0 & 0 & 1 & 1 & 0 & 0 & 0 & 0 & 1 & 1 & 0 & 0 & 1 & 1 \\ 1 & 1 & 1 & 0 & 1 & 1 & 1 & 0 & 1 & 1 & 1 & 0 & 0 & 0 & 0 & 1 \\ 1 & 0 & 0 & 0 & 0 & 1 & 1 & 1 & 0 & 1 & 1 & 1 & 0 & 1 & 1 & 1 \\ 1 & 1 & 1 & 0 & 1 & 1 & 1 & 0 & 0 & 0 & 0 & 1 & 0 & 0 & 0 & 1 \\ 1 & 1 & 0 & 0 & 1 & 1 & 0 & 0 & 0 & 1 & 1 & 0 & 0 & 0 & 0 & 1 \\ 1 & 1 & 0 & 0 & 0 & 0 & 1 & 1 & 0 & 0 & 1 & 1 & 0 & 0 & 1 & 1 \\ 1 & 0 & 0 & 0 & 1 & 0 & 0 & 0 & 0 & 1 & 1 & 1 & 0 & 1 & 1 & 1 \\ 1 & 1 & 1 & 0 & 0 & 0 & 1 & 0 & 0 & 0 & 1 & 0 & 0 & 0 & 1 & 1 \\ 1 & 0 & 0 & 0 & 1 & 0 & 0 & 0 & 1 & 0 & 0 & 0 & 0 & 1 & 1 & 1 \end{pmatrix} \quad (3)$$

After solving this system of linear equations we can finally map the impurity distribution across the flake and this is shown on the right part of Table I in the main manuscript. The table shows the real occupation of impurities for all sixteen cells together with the sudoku-style solutions. The deviation between them never exceeds two impurities.

In the first part of this SM we showed how flexible this inversion technique is to the extent that we may obtain the spatial distribution of impurities on a 2D flake in a few different ways. With this in mind, we now illustrate yet another way in which the impurity distribution can be spatially mapped, this time using electrodes of different lengths. In the main manuscript we considered electrode leads that spanned the entire length of the flake on each side. We subsequently considered the case in which the electrodes were reduced in size but both injecting and extracting electrodes were always identical in sizes. We now relax this constraint and assume that electrodes have different dimensions, which we refer to as the hybrid approach. A schematic representation of this can be seen in Fig.5 where one lead spans the entire width of the flake whereas the other is either half or a quarter of the length of its counterpart. Here we follow similar steps to the ones taken previously and find exactly the same results as the ones found in Fig.1 of the main manuscript. In fact, Fig. 6 displays the misfit functions plotted as a

function of impurity numbers in the entire flake using leads in magenta and green colors. Although the functions are different, both display a distinctive minimum

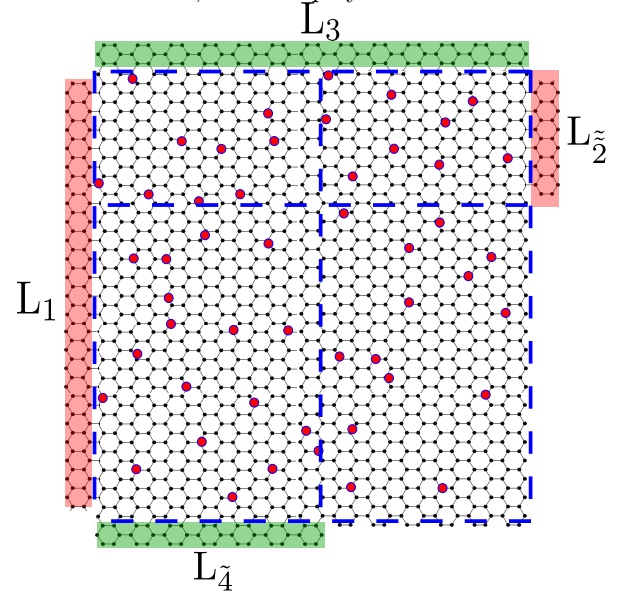


FIG. 5. A schematic presentation of the hybrid approach where one lead spans entire width of the and another electrode of quarter length or half length of its counterpart.

at the same value of $N = 50$. In the inset another two misfit functions are plotted with minima indicating the occupation of the top row (red) and left half (blue) of the flake indicated with the dashed lines of Fig. 5.

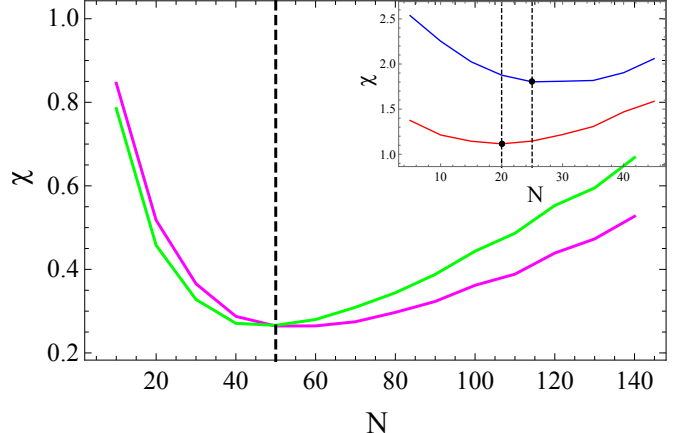


FIG. 6. Misfit function plotted in blue color is defined using input signal $\mathcal{T}_{3,\tilde{4}}$ scans left half of the device. Misfit function defined using $\mathcal{T}_{1,\tilde{2}}$ yields occupation of row constrained by pink leads and dashed blue lines .